Omnidirectional Monolithic Marker for Intra-Operative MR-Based Positional Sensing in Closed MRI

Chim-Lee Cheung, Mengjie Wu, *Graduate Student Member, IEEE*, Ge Fang, Justin D. L. Ho, Liyuan Liang, Kel Vin Tan, Fa-Hsuan Lin, Hing-Chiu Chang, and Ka-Wai Kwok, *Senior Member, IEEE*

***Abstract*— We present a design of an inductively coupled radio frequency (ICRF) marker for magnetic resonance (MR)-based positional tracking, enabling the robust increase of tracking signal at all scanning orientations in quadrature-excited closed MR imaging (MRI). The marker employs three curved resonant circuits fully covering a cylindrical surface that encloses the signal source. Each resonant circuit is a planar spiral inductor with parallel plate capacitors fabricated monolithically on flexible printed circuit board (FPC) and bent to achieve the curved structure. Size of the constructed marker is Ø3-mm × 5-mm with quality factor > 22, and its tracking performance was validated with 1.5 T MRI scanner. As result, the marker remains as a high positive contrast spot under 360° rotations in 3 axes. The marker can be accurately localized with a maximum error of 0.56 mm under a displacement of 56 mm from the isocenter, along with an inherent standard deviation of 0.1-mm. Accrediting to the high image contrast, the presented marker enables automatic and real-time tracking in 3D without dependency on its orientation with respect to the MRI scanner receive coil. In combination with its small form-factor, the presented marker would facilitate robust and wireless MR-based tracking for intervention and clinical diagnosis. This method targets applications that can involve rotational changes in all axes (X-Y-Z).**

***Index Terms*— Magnetic resonance imaging (MRI), positional tracking, inductively coupled radio frequency (ICRF) coil, interventional MRI, position measurement.**

Manuscript received 25 June 2023; revised 16 August 2023; accepted 20 August 2023. Date of publication 30 August 2023; date of current version 2 January 2024. This work was supported in part by the Innovation and Technology Commission (ITC) of Hong Kong under Grant MRP/029/20X and Grant ITS/403/18; in part by the Multi-Scale Medical Robotics Center Ltd., InnoHK; and in part by the Research Grants Council (RGC) of Hong Kong under Grant 17207020, Grant 17205919, Grant 17209021, Grant 17125321, Grant 17106820, and Grant T42-409/18-R. *(Chim-Lee Cheung and Mengjie Wu are co-first authors.) (Corresponding author: Ka-Wai Kwok.)*

Chim-Lee Cheung, Mengjie Wu, Ge Fang, and Justin D. L. Ho are with the Department of Mechanical Engineering, The University of Hong Kong, Hong Kong (e-mail: zardchim@connect.hku.hk; u3008064@connect.hku.hk; fangge@connect.hku.hk; jdlho@connect.hku.hk).

Liyuan Liang and Hing-Chiu Chang are with the Department of Biomedical Engineering, The Chinese University of Hong Kong, Hong Kong, and also with Multi-Scale Medical Robotics Center Ltd., Hong Kong (e-mail: liangly0507@gmail.com; hcchang@hku.hk).

Kel Vin Tan is with the Department of Diagnostic Radiology, The University of Hong Kong, Hong Kong, and also with the Department of Oncology, University of Oxford, OX3 7DQ, Oxford, U.K. (e-mail: kelvintan.kvt@gmail.com).

Fa-Hsuan Lin is with the Department of Medical Biophysics, University of Toronto, Toronto, ON M5G 1L7, Canada, and also with Sunnybrook Research Institute, Toronto, ON M4N 3M5, Canada (e-mail: fhlin@sri.utoronto.ca).

Ka-Wai Kwok is with the Department of Mechanical Engineering, The University of Hong Kong, Hong Kong, and also with Multi-Scale Medical Robotics Center Ltd., Hong Kong (e-mail: kwokkw@hku.hk).

This article has supplementary downloadable material available at https://doi.org/10.1109/TMI.2023.3309967, provided by the authors.

Digital Object Identifier 10.1109/TMI.2023.3309967

I. Introduction

ACHIEVING accurate localization and positional tracking of interventional tools and patient anatomy under MRI plays a critical role in MR-guided intervention and clinical diagnosis [1]. Development in MR markers has enabled precise targeting and control during surgical operation, such as biopsy procedure [2], neurosurgery [3], renal denervation [4], and brachytherapy [5] etc. Furthermore, the markers also introduced solutions in automatic three-dimensional location [5], [6], [7], [8], [9] and motion artifact reduction [6], [10].

Based on the structure and working principle, these markers can be categorized into *passive-*, *active-*, *semi-active*, and *tuned-circuit* tracking. Passive tracking markers contain contrast agents that alter local MR signal intensity by shortening T1 or T2 value [11], [12], or paramagnetic materials that introduce local magnetic field distortion [13], [14], [15]. Although *passive* marker can avoid RF safety hazards, it generally involves complicated MR sequences to identify marker signal unambiguously from background signals [16], or distinguish signals from multiple markers when they are closed to each other. *Active* tracking marker utilizes MR-compatible radiofrequency (RF) circuits wired to MR scanner. The major advantage of active marker is that fast and accurate tracking can be conducted with multiple markers connected to the scanner receiver channels. However, the long electrically conductive wire connection would induce RF heating [17], [18], [19], [20], [21], or pose a barrier in clinical or interventional implementations [17], [22], [23]. *Semi-active* tracking was proposed and replaced the electrically conductive wires by an optical fiber [23], [24]. The fiber can switch the resonant frequency of the resonant circuit through controlling the amount of light transmit to a photodiode or photoresistor. However, these extra electronic components inevitably increase the overall size of marker, thus making integration further difficult.

To this end, inductively coupled radio frequency (ICRF) markers have gained increasing interest for MR-based tracking [2], [6], [8], [25], [26], [27], [28], [29], [30], [31], as they do not require electrically conducting wire connection to the MRI scanner, thus reducing the implementation complexity, as well as the risk of RF-induced heating due to wiring [17], [18], [19]. Furthermore, by using 1D-projection MRI pulse sequence, wireless markers can offer real-time tracking with high signal-noise-ratio at around 30 Hz [6], [30]. The underlying working principle of wireless tracking is resonant inductive coupling between the marker's inductor and MRI RF coils such that the excitation magnetic field inside the marker can be substantially increased. Therefore, it increases the flip angle and MR signal during the RF excitation and MRI data acquisition, respectively, thus giving rise to image contrast surrounding the marker. Recent advances in ICRF marker design have led to smaller footprints with high quality factor [32], e.g., using 3-D circuits printed with aerosol jet deposition [33]. Celik et al. [8] also presented MR-tracking of both position and orientation just using a single marker. Remote-control schemes [2] were also proposed by employing optical or electrical triggers, altering the RF resonance properties [34] of ultra-thin and flexible marker for anatomic marking.

The design approaches of resonant circuits can be categorized into *solenoid* coil [6], [9], [29], [35], [36], [37], *planar* coil [8], [30], [32], [38], *double helix* inductor [33], and *split-ring* structures [2]. However, the majority of their designs [2], [6], [8], [28], [29], [30], [32], [34] encountered the same problem of orientation dependency, such that the signal-noise-ratio drops to its minimum when the inductor surface normal aligns to the MRI static magnetic field. This is because the degree of magnetic flux coupling, and hence the level of signal increase has orientation dependency. Pairs of resonant circuits with crossed solenoid inductors were previously proposed, acting as fiducial markers for catheter tracking. However, it is technically challenging to fabricate solenoid inductors in small diameter. Manual winding may not make it possible, and the required tuning and matching processes could also be tedious and complicated. Therefore, in this study, we present a new method that overcomes the existing challenges in signal orientation dependency as well as fabrication difficulty. Our approach utilizes a monolithic flexible printed circuit (FPC) board fabricated with three curved resonant circuits, to enable wireless 3D positional tracking with strong signal increase at all orientations.

Our work contributions can be summarized below:

i) It is the *first* MR tracking marker utilizing curved monolithic structures for omnidirectional sensing. The bendable tracking marker allows mutual coupling between the marker and MRI $\mathbf{B}_1$ field at ANY orientation.
ii) Fabrication of a curved marker with flexible printed circuit (FPC), where its monolithic structure enables full machine manufacturing without tedious manual tuning and matching.
iii) Performances of marker imaging and localization were evaluated under a closed-bore 1.5 T MRI scanner. Orientation dependency and tracking performance of the marker are both evaluated. RF-induced heating of our fabricated markers is also verified to ensure MR safety.

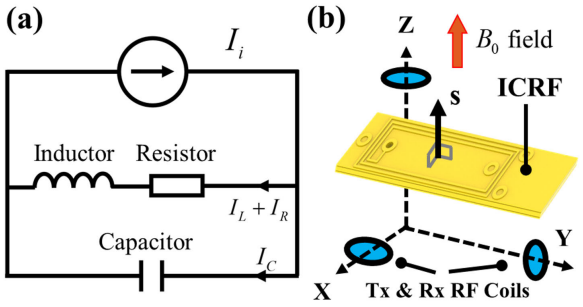

Fig. 1. (a) Schematic diagram of a typical ICRF coil circuit. Current, I, generated through inductive coupling between resonant circuit and MR scanner RF coils. (b) Orientation of an inductively coupled radio-frequency marker (ICRF) with respect to MRI $\mathbf{B}_0$ field, Tx and Rx RF coils. A circularly polarized B_1 field is generated and received on the X-Y plane. Surface normal of the marker inductor is denoted by vector **s**.

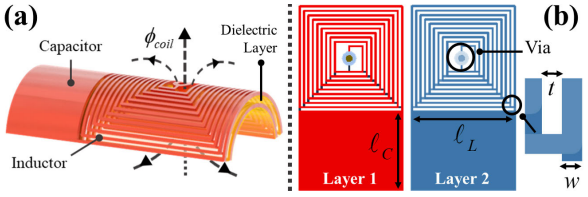

Fig. 2. (a) Architecture of an individual resonant circuit. The circuit inductively couples to the scanner RF Tx and Rx coils in order to increase the MR signal. (b) Copper conductor routing demonstrations with number of turns: 9, $\ell_L = 2.8$ mm, $\ell_C = 2$ mm, $w = 0.06$ mm, $t = 0.06$ mm.

II. Material and Methods

In the present study, our aims are 1) to track and visualize the marker in arbitrary orientations around the X-, Y- and Z- axis, and 2) to increase and visualize MR signals with the marker at low flip angle (i.e., 1°) such that only signal sources near the marker are excited, and allows rapid localization of the wireless marker using 1D projection, precluding the need for time-consuming image reconstruction [29], [30].

A. Orientation Dependency in Prior Art

A wireless marker is a tuned LC tank circuit (**Fig. 1a**) at resonant frequency matchable with the MRI scanner Larmor frequency. When a wireless marker is placed inside a closed-bore scanner with circularly polarized $\mathbf{B}_1$ field, only components B_1^+ and B_1^- that are parallel to the marker's surface normal vector **s** are effective for generating current through its inductor. Referring to **Fig. 1b**, when surface normal **s** moves along the X-Y plane, the signal is constant as the effective flux passing through the marker surface is the same. However, when **s** is parallel to the Z-axis, the electromagnetic coupling between the inductor and Tx/Rx RF coils becomes zero and no signal enhancement can be achieved.

B. Omnidirectional Marker Design

The marker comprises of three resonant circuits where each circuit is formed by arranging two layers of conductive copper paths into a planar spiral inductor, with a central via connecting the planar inductors together, as illustrated in **Fig. 2a-b**. The spiral inductor is then connected to a parallel plate capacitor to form an LC tank circuit. The capacitor is designed by sandwiching a dielectric layer (material: polyimide, thickness: 25 μm) between two conductive plates on

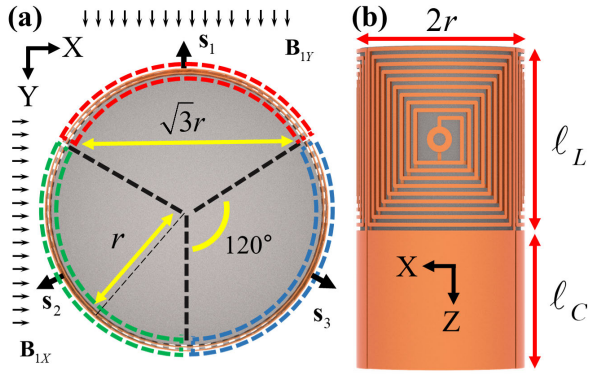

Fig. 3. Omnidirectional marker: (a) Front view. Three curved resonant circuits are located by red, blue and green dash-line regions. The surface normals of three individual circuits are $\mathbf{s}_1$, $\mathbf{s}_2$ and $\mathbf{s}_3$. (b) Top view.

both sides of a flexible printed circuit (FPC). A standard FPC fabrication process [39] was used to electroplate the copper as the conductive layer (thickness: 12 μm), with an electrically insulative coverlay encapsulating the circuit. It involves circuit pattern exposure, etching, copper plating and coverlay lamination. 3D-printed circuit fabrication could also be considered with precise inkjet deposition printer (e.g., Nano Dimension DragonFly LDM 2.0 [40]). The proposed marker architecture is a monolithic structure where the inductor and capacitor are connected to each other during machine manufacturing, and no manual fabrication is needed.

The omnidirectional tracking arrangement is shown in **Fig. 3a-b**, with three curved resonant circuits evenly wrapped on a 3 mm diameter hollow cylinder (wall thickness: 0.25 mm, length: 10 mm) surface, such that the three circuits' surface normal $\mathbf{s}_1$, $\mathbf{s}_2$ and $\mathbf{s}_3$ originated from the same centroid are separated by 120° along the same plane. The length ℓ_L of inductor can be briefly expressed as:

$$\ell_L = \frac{2r\pi}{3} \tag{1}$$

where r is the radius of central cylinder as shown in **Fig. 3**. A gap of 0.2 mm was reserved between circuits to avoid electrical bridging during fabrication. An individual resonant circuit has a total dimension of 2.8 mm × 5 mm in planar form. The cylinder is filled with 10 mM gadolinium-doped water which is a typical MRI contrast agent for enhancing signal increase, acting as the internal signal source. Two sides of the cylinder were sealed with UV-curable adhesive.

A wireless marker couples to scanner RF coils in two modes [23], [37]: in transmit mode, the marker couples to transmit coil $\mathbf{B_1}$ field during RF excitation, generating additional flux that increases flip angle. And in receive mode, reciprocal effect takes place and the observed signals by receiver coil are increased. The flux generated in the marker can be expressed as

$$\phi = \mathbf{B_1} A \tag{2}$$

where A refers to the marker surface area that can be coupled to the scanner RF coils. The marker surface area A can further be decomposed into two perpendicular plane areas A_x and A_y. As illustrated in **Fig. 4**, angles $\theta_{X'}$, $\theta_{Y'}$, and $\theta_{Z'}$ denote the rotation around X'-, Y'-, and Z'-axis, respectively.

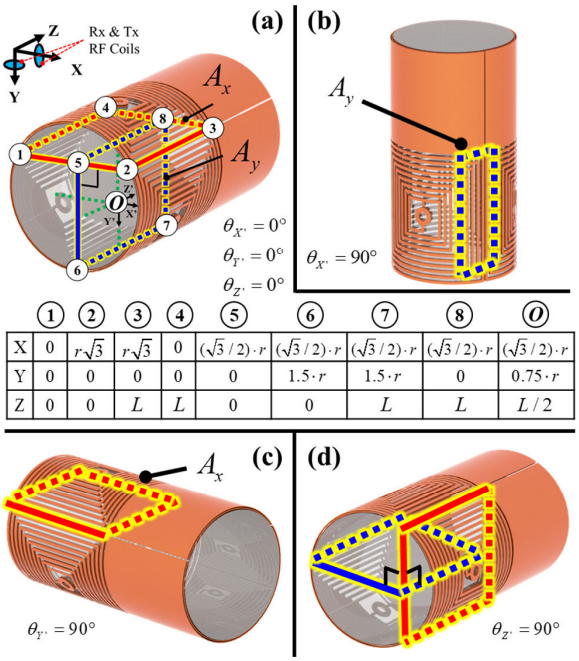

	1	2	3	4	5	6	7	8	O
X	0	$r\sqrt{3}$	$r\sqrt{3}$	0	$(\sqrt{3}/2)\cdot r$	$(\sqrt{3}/2)\cdot r$	$(\sqrt{3}/2)\cdot r$	$(\sqrt{3}/2)\cdot r$	$(\sqrt{3}/2)\cdot r$
Y	0	0	0	0	0	$1.5\cdot r$	$1.5\cdot r$	0	$0.75\cdot r$
Z	0	0	L	L	0	0	L	L	$L/2$

Fig. 4. Marker's effective planes for $\mathbf{B_1}$ field to pass through during RF excitation and acquisition at two perpendicular orientations: planes A_x (red), and A_y (blue). Their corners are labeled by 8 numbers along with the origin point, O. The corners' 3D coordinates are tabulated below. (a) Marker with $\theta_{X'}$, $\theta_{Y'}$, $\theta_{Z'} = 0$. Plane A_x lies on X-Z plane, and plane A_y on Y-Z plane. (b) When $\theta_{X'} = 90°$, the marker is positioned vertically, thereby only plane A_y is effective for $\mathbf{B_1}$ field to pass through. (c) When $\theta_{Y'} = 90°$, only plane A_x is effective. (d) When $\theta_{Z'} = 90°$, both the planes A_x (red) and A_y (blue) are effective.

When angles $\theta_{X'}$, $\theta_{Y'}$ and $\theta_{Z'}$ are equal to zero, the planes, A_x and A_y are orientated as depicted in **Fig. 4a**, and their surface area can be expressed as:

$$\begin{aligned} A_x &= \sqrt{3}\cdot r\cdot \ell_L \\ A_y &= 1.5\cdot r\cdot \ell_L \end{aligned} \tag{3}$$

Note that for readily expression, the gaps (0.2 mm) among adjacent resonant circuits are assumed negligible. Effective area H_{eff} for inductively coupling in three different boundary conditions (i.e. $\theta_{X'} = 0, \theta_{Y'} = 0, \theta_{Z'} = 0$) shown in **Fig. 4a-d**, can be expressed as:

$$\begin{aligned} H_{eff}(\theta_{X'}) &= 2A_x\cos(\theta_{X'}) + 2A_y \\ H_{eff}(\theta_{Y'}) &= 2A_x + 2A_y\cdot\cos(\theta_{Y'}) \\ H_{eff}(\theta_{Z'}) &= 2A_x + 2A_y \end{aligned} \tag{4}$$

Note that the effective area at any orientation is always larger than zero, allowing it to receive and increase MR signals at arbitrary angle.

C. Marker Fabrication and Characterization

Three resonant circuits were fabricated monolithically in a single piece form (**Fig. 5a**). In our case, only the length ℓ_C of capacitor, as shown in **Fig. 3**, is variable, while the planar square inductor size, the thickness and dielectric constant of dielectric layer are all fixed. Therefore, the single circuit can be fine-tuned by only adjusting the length ℓ_C of capacitor in our few design iterations. However, when three circuits were wrapped evenly on the hollow cylinder

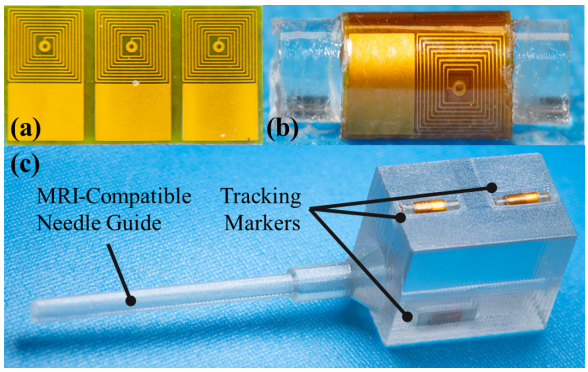

Fig. 5. (a) Original planar form of three monolithic resonant circuits. (b) Curved form of the resonant circuits forming the omnidirectional marker. (c) Three markers embedded inside an MRI-compatible needle guide in order to provide 6-DOF positional tracking.

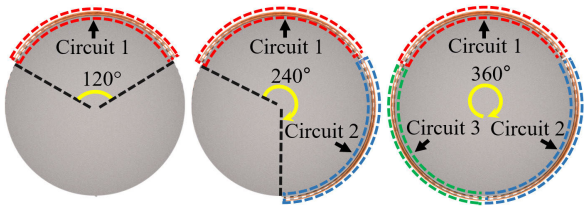

Fig. 6. Three markers wrapped around the surface of a glass tube. The number of circuits differs for each marker: 1, 2, and 3.

to form the marker (**Fig. 5b**), deformation could change the resonant frequency of each circuit. The resonant modes of final assembly are contributed by three circuits and their mutual coupling effect together, complicating the frequency tunning. Moreover, identical resonant circuits placed adjacently can lead to frequency splitting. To accurately quantify the coupling effect, we carried out an S12 measurement experiment and finite element analysis (FEA). As shown in **Fig. 6**, two new baseline markers were fabricated to compare their frequency response with our 3-circuit marker, which can show how the resonating modes change as the number of circuits increases. One baseline contains one circuit, and the other contains two circuits. The gap between the two circuits remained at 0.2 mm. All these circuits were also wrapped around the surface of the cylindrical glass tube (Ø3 mm). The frequency response of three markers was characterized using a vector network analyzer (E5071C, Keysight Technologies). A non-contact probing setup with an electric field probe (100D, Beehive Electronics) and a magnetic field probe (100A, Beehive Electronics) was connected to E5071C for wireless measurement [32]. The measurement mode of E5071C was configured as S12. Furthermore, COMSOL Multiphysics® (COMSOL Inc, Sweden) was used to simulate the inductive coupling among three circuits. The marker was placed in a spherical air domain with a diameter of 16 mm. The air domain was wrapped by a 1.5 mm-thick perfect match layer (PML), reducing the interference caused by boundary reflections. The material of the dielectric layer was polyimide, and its relative permittivity was 3.4. In the mesh construction, the minimum element size was set as 3 μm for some significant parts (e.g., via, copper layer and dielectric layer), so the smallest surface can be divided into four mesh cells. As shown in **Fig. 7**, the model was divided into 7,396,888 free

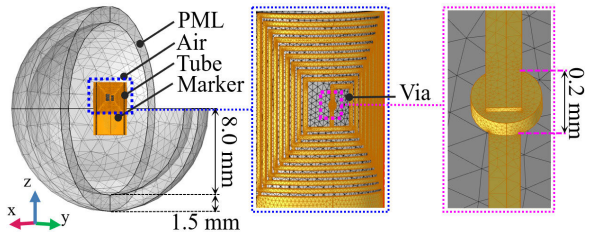

Fig. 7. Finite element mesh construction in the case of free tetrahedral elements in COMSOL Multiphysics. Three circuits (yellow) are attached to a glass tube and placed in the center of a spherical air domain (Ø16 mm). A 1.5 mm-thick perfect match layer (PML) wraps outside the air domain, serving as an open and non-reflecting infinite magnetic domain. A finer mesh scale (minimum element size: 3 μm) is applied to these crucial parts (e.g., the via) to ensure sufficient mesh resolution.

tetrahedral elements and 1,279,610 boundary elements to ensure a high mesh resolution for FEA simulation. Because the self-inductance and mutual inductance among three resonators are solely dependent on the marker's geometry and independent of the currents' values [41], three circuits are directly excited by input currents to simulate the induced magnetic field. As depicted in **Fig. 9b**, specifying a 180° intersection angle between virtual RF waves and the Y-axis, RF waves traverse circuit 1 from outer surface to inner surface, and then traverse circuit 2 and 3 in opposite directions. Thus, the input currents in circuit 2 and 3 have the same direction, opposing to the current direction of circuit 1. In addition to the current direction, the input current values must be proportional to the effective areas defined in **Equation (4)**, where the circuit 1 effective area is twice that of circuit 2 or 3. Therefore, in our COMSOL mode, circuit 1 was stimulated by a current of -0.8 milliamps, whereas the remaining two circuit units were excited by 0.4 milliamps. Note that these currents' values and polarity are not the actual currents generated in MR experiment. Then, we conducted three studies in COMSOL AD/DC module: 1) simulation of the capacitance (C) in Electrostatic Field Interface; 2) simulation of self-inductance (L), mutual inductance (M) as well as resistance (R) of the circuits in Magnetic Field Interface; 3) study of frequency response using the Electric Circuit Interface to connect R, L, M, and C. For ease of reproducible prototyping, we have shared the COMSOL-based 3D FE model, original project, and the Gerber files of our FPC on a public GitHub repository (https://github.com/mengjwu/MRtrackingMarker). Note that these three circuits have to be assembled on glass cylinder tube filled with 10 mM Gd-doped water that acts as internal signal source. To evaluate maker's signal increase effect in addition to the positive contrast agent, two cylinders with same size and amount of 10 mM gadolinium-doped water were scanned with and without marker, at flip angle $= 1°$ and flip angle $= 10°$ respectively. The MR images were acquired using fast spoiled gradient-echo (FSPGR) sequence, with parameters: TE $= 2.788$ ms, TR $= 7.1$ ms, Slice thickness $= 30$ mm, Matrix $= 192 \times 192$, Pixel Spacing $= 0.75$ mm. The signal increase effect was also evaluated against the relative distance between marker and scanner receive coil, where the body coil in MR scanner acted as Tx coil, and the birdcage coil served as Rx coil. Both of the Tx and Rx coils used quadrature polarization. Marker signal-noise-ratio (SNR) was

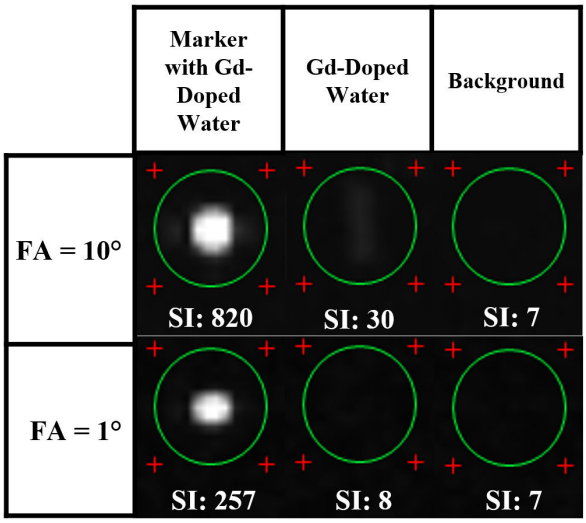

Fig. 8. Coronal images of cylinder with marker and Gd-doped water, and Gd-doped water only. The bright spot both at flip angle (FA) = 1° and 10° indicates the signal increase effect of the marker. Region of interest maximum signal intensities (SI) of highlight green region indexed.

compared between two placements: one is at the isocentre of MR scanner, and the other is on the inner surface of receive coil so as to ensure the minimal relative distance from the coils. The MR images were acquired using a GE Signal Artist scanner with FSPGR sequence, with parameters: TE = 3.3 ms, TR = 7.2 ms, Slice Thickness = 20 mm, Pixel Spacing = 1 mm, Flip Angle = 1°.

D. MRI Orientation Dependency Test

The marker orientation dependency was evaluated with the marker embedded inside a 3D-printed MRI compatible block. The block is mounted on a 3D-printed plastic protractor stand that can rotate in steps of 10° around X'-, Y'- and Z'- axis from 0° to 90°. The protractor stand was affixed at the isocenter inside a clinical 1.5 T MRI Scanner (Signa Explorer, GE Healthcare) with a standard 8-receiver imaging head coil. The marker filled with 10 mM gadolinium-doped water is sufficient to generate enough signal to be detected by the receive coil. Apart from gadolinium-doped water and the subject inside the head coil, no extra signal source was present during the experiments even at low flip angle (e.g., 1°).

The MR images at different orientations were acquired using FSPGR sequence, with parameters: TE = 2.144 ms, TR = 7.185 ms, slice thickness = 2 mm, matrix = 200 × 200, flip angle = 1°, FOV = 120 mm × 120 mm, pixel spacing = 0.6 mm. Image distortion caused by gradient nonlinearities was compensated with gradient warp correction. DICOM images were extracted and processed in MATLAB.

E. MRI Tracking Accuracy and Precision Test

The marker was placed successively at 28 positions on a standard 16 × 16 Lego plate. The Lego plate has an 8-mm step size and precision of 5 μm, and was fixed inside the head coil with adhesive and aligned with MRI scanner positioning laser. One-dimensional (1D) gradient readouts with non-spatially-selective RF excitation [42] was employed to retrieve MR projection signal of the marker, and additional dephasing gradients were applied to suppress residual background signal (TR = 8.7 ms, TE = 2.04 ms, Flip Angle = 1°,

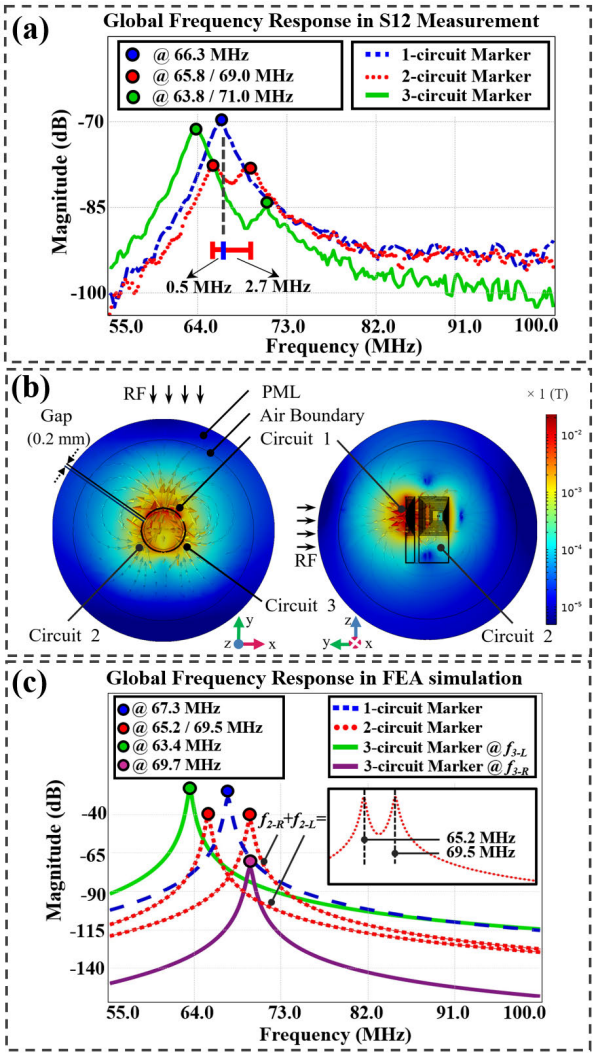

Fig. 9. Experimental measurement and FE simulation results. (a) Global frequency response of three markers in S12 measurement experiment. The 1- and 2-circuit configurations act as baseline for comparison. (b) Top-view and lateral-view induced magnetic field of our 3-circuit marker in COMSOL, referring to the layers setting in Fig. 7. The RF source excites the marker along the reverse direction of the Y-axis. The warmer color refers to the higher magnetic flux density. (c) COMSOL-based global frequency response of three markers as shown in Fig. 6. Green and purple solid curves form the global response of our proposed 3-circuit marker, revealing a pronounced resonant strength (−25 dB) at Larmor frequency in comparison with the right splitting peak (−70 dB).

FOV = 192 mm, Pixel spacing = 1 mm, Slice Thickness = 300 mm). Thirty MR scans were conducted initially to acquire baseline data for later comparison. MR signals were captured with the marker moved along the X- and Z- direction of the plate at step sizes of 8 mm. We assumed X- and Y-coordinates share the same positional errors, as the gradient and RF coils have principal symmetry with respect to X and Y axes. Therefore, Y-direction data was not measured separately.

Marker accuracy and precision were evaluated with the sub-pixel localization method [43] from scanned projection data, in which the marker positions were calculated with intensity linear interpolation (ILI). This method searches for two coordinates with intensities equal to half of the peak value along one axis initially, and calculates the marker center coordinate through averaging.

F. MR Imaging and Radiofrequency Safety Test

MR experiments were conducted to validate capability for visualizing subjects and instruments in a single MRI image. The 3D-printed MRI compatible block used in the orientation dependency test, and an MRI-compatible needle guide [3] (**Fig. 5c**) embedded with three markers were mounted on the forehead of the subject who was scanned with supine position. Fast gradient echo pulse sequence (TE = 2.692 ms, TR = 5.853 ms, slice thickness = 1 mm, matrix = 256 × 256, pixel spacing = 1 mm) was applied to retrieve MR images on the aforesaid 1.5 T MRI scanner. Real-time localization of two markers was also tested. We mounted the markers on a plate which was moved/rotated by a robotic platform. The plate motion was actuated in an arbitrary trajectory, and driven by our developed MR-safe fluid transmission system [44]. The aforementioned MR one-dimensional (1D) projection pulse sequence was also employed to track the markers motion.

The tracking marker can resonate during $\mathbf{B_1}$ RF excitation and cannot be switched on or off remotely; Therefore, it is possible to induce current that can generate RF heating that is potentially hazardous to humans. Marker temperature was measured and logged with 2 fiber-optic fluorescent temperature sensor system with 0.01 degree Celsius resolution (PRB-MR1 OSENSA, Canada). One sensor was affixed to a circuit's top surface to measure temperature directly, and another one was affixed to the MRI scanner table as environmental temperature reference [2], [5], [6], [30], [45]. The sensors were channeled through the scanner room waveguide and connected to a computer and measurement logging unit (FTX-300-LUX+, OSENSA, Canada). To reduce thermal influence from environment, in our test, a blanket acting as thermal insulator was put on the whole setup. In prior to the MRI scanning, the setup was placed still in scanner room for 15 minutes to ensure the setup has reached steady state temperature as the room.

As the closed scanner utilizes quadrature coils, the $\mathbf{B_1}$ transmit field is homogeneous inside the birdcage type receive coil [46]. In this case, the position of marker is irrelevant to the RF heating effect. The worst-case condition can be considered when a high RF-duty sequence was adjusted with whole-body averaged specific absorption rate (SAR) at 2 W/kg [1], [2], [3]. The pulse sequence and parameters were used to mimic the worst-case condition, such that the whole-body SAR of 2 W/kg could be induced for 15 minutes. Fast-spin echo imaging sequence (TE = 9.26 ms, TR = 500 ms, ETL = 36, slice thickness = 20 mm, Matrix = 512 × 512, FOV = 410 mm × 410 mm, and flip angle = 180°) was repeated for 15 minutes on the 1.5 T MRI scanner to induce a whole-body average specific absorption rate (SAR) of 2 W/kg [30].

III. Results and Discussions

A. Marker Characterization

Fig. 8 shows the marker can increase the MR signal by about 32 and 27 times than Gd-doped water, respectively, at FA = 1° and FA = 10°. **Fig. 9a** displays the global frequency response of three markers in S12 measurement, i.e., 1-circuit, 2-circuit, and our 3-circuit marker. The 1-circuit baseline marker (dashed blue) resonates at the eigenfrequency (f_0) of 66.3 MHz. Then, the frequency splitting is observed on the 2-circuit baseline marker (dotted red), where the right peak increases to 69.0 MHz (f_0 + 2.7 MHz), and the left peak decreases to 65.8 MHz (f_0 − 0.5 MHz). Solid green curve represents the global frequency response of our 3-circuit marker, where the left peak reduces further to 63.8 MHz (f_0 − 2.5 MHz), and the right peak continues to rise to 71.0 MHz (f_0 + 4.7 MHz). However, the right peak's magnitude (−83 dB) is significantly lower than the left (−72 dB), which differs from these two splitting peaks observed in 2-circuit marker. It is noted that some works [47], [48] have also shown that the resonating magnitude of two splitting peaks may not be equal or even close. Despite the presence of frequency splitting, the results shown in **Fig. 8** have demonstrated the successful signal increase effect of our 3-circuit marker. **Fig. 9b** illustrates the magnetic flux density and direction of magnetic lines in COMSOL. The arrows indicate that the direction of magnetic lines, and the warmer color around circuit 1 indicates stronger magnetic field strength. This 3D magnetic field distribution is contributed by three circuits and their coupling effect. FEA computes three self-inductance and six mutual inductance parameters, and expresses them as a matrix Lm(units in μH).

$$Lm = \begin{bmatrix} 0.8536 & 0.0552 & 0.0552 \\ 0.0552 & 0.8536 & -0.0552 \\ 0.0552 & -0.0552 & 0.8536 \end{bmatrix} \tag{5}$$

where i and j are index of the primary circuit and secondary circuit; $Lm_{(i,j)}, i = j$ is the self-inductance of the i^{th} circuit; $LM_{(i,j)}, i \neq j$ is the mutual inductance between i^{th} and j^{th} circuit. Three identical diagonal elements of the matrix Lm represent the self-inductance of three uniform circuits. Because of the spatial symmetry of our marker, the absolute values of non-diagonal elements are identical, yielding the matrix symmetric as in **Equation (5)**, with plus/minus signs to indicate the mutual coupling polarity. **Fig. 9c** shows the FEA-based global frequency response of three markers, where Y-axis represents the resonating magnitude (units in dB), and X-axis represents the frequency (units in MHz). The dashed and dotted lines correspond to the global frequency response curves of the 1-circuit and 2-circuit markers, respectively, while two solid lines represent that of our 3-circuit marker. The green solid line denotes the left resonating mode ($f_{3-\text{L}}$), and the purple represents the right mode ($f_{3-\text{R}}$). The 1-circuit marker receives no coupling and resonates at the eigenfrequency of 67.3 MHz, which is close to the eigenfrequency (66.3 MHz) measured in S12 experiment. However, due to the mutual coupling of the 2 circuits, frequency splitting phenomenon occurs on the 2-circuit marker, and two central frequencies are derived as follows [49], [50],

$$\begin{aligned} f_{2-\text{L}} \times 2\pi\sqrt{C \times (Lm_{(1,1)} + Lm_{(1,2)})} &= 1 \\ f_{2-R} \times 2\pi\sqrt{C \times (Lm_{(1,1)} - Lm_{(1,2)})} &= 1 \end{aligned} \tag{6}$$

where $f_{2\text{-L}}$ and $f_{2\text{-R}}$ is the 2-circuit's left and right central frequency, respectively; and C is the capacitance of single circuit, with a computed value of 6.5264 pF by FEA. The left peak at 65.2 MHz is asymmetric to the right at 69.5 MHz, with respect to the eigenfrequency (67.3 MHz).

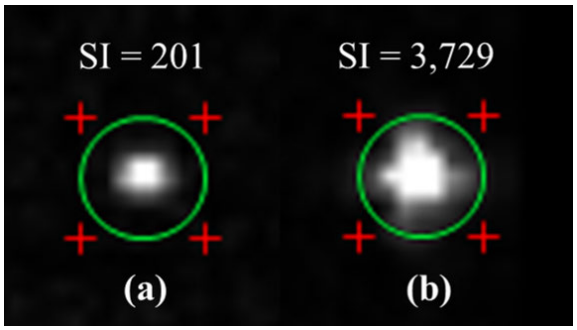

Fig. 10. Coronal images of marker (a) placed at scanner isocenter, and (b) attached onto the receive coil inner surface. Region of interest is enclosed by a green circle, the pixels with maximum signal intensity (SI) inside the regions are 201 and 3,729.

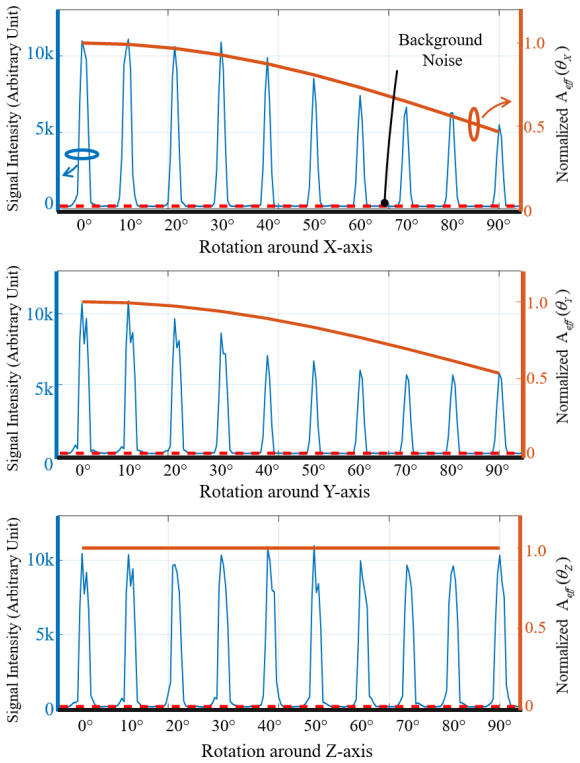

Fig. 11. Increased MR signal profile plot in different orientations. Background noise is indicated with red dash lines. The change in signal intensities is approximately the same as the effective area modelling in Equation (4).

The profile of $f_{2\text{-L}} + f_{2\text{-R}}$ highly matches the 2-circuit baseline marker's response curve in **Fig. 9a**. With the addition of the third circuit, the mutual coupling involved in the 3-circuit marker becomes more complicated [51]. The resonant frequencies f can be derived from **Equation (7)** [51], [52].

$$K_{ij} \times \sqrt{Lm_{(i,i)} \times Lm_{(j,j)}} = Lm_{(i,j)}$$
$$(1-\lambda)^3 - (1-\lambda)(K_{12}^2 + K_{23}^2 + K_{13}^2) + 2K_{12}K_{23}K_{13} = 0$$
$$f \times \sqrt{\lambda} = f_0 \tag{7}$$

where K_{ij} is the coupling coefficient between the i^{th} and j^{th} circuit. The eigenvalue λ of the cubic equation usually has three solutions, resulting in three resonant modes for a common 3-circuit marker [52]. The solutions are (1.1293, 0.9353, 0.9353), where λ_1 corresponds to the first eigenvalue 1.1293, λ_2 and λ_3 are identical. This provides a theoretical explanation for why the proposed 3-circuit marker exhibits only two resonant modes. The calculated frequency of left mode ($f_{3\text{-L}}$) is 63.4 MHz, and the right ($f_{3\text{-R}}$) resonates at 69.7 MHz, closely matching the global frequency response

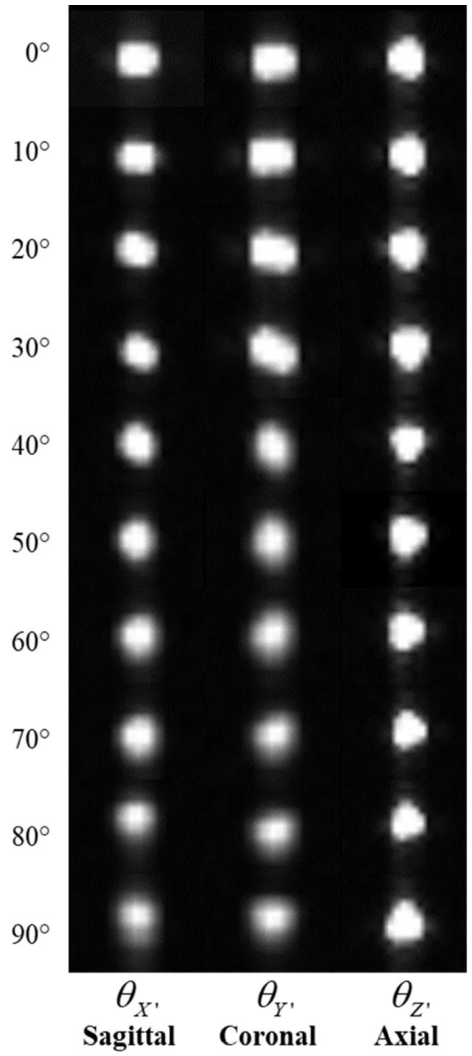

Fig. 12. Sagittal, coronal, and axial gradient echo images of the marker at low flip angle (1°) acquired at ten different orientations using a fast spoiled gradient-echo (FSPGR) sequence. Marker signal can be unambiguously identified from the background at any orientation. The max. and min. signal-to-background ratio are, respectively, around 57 and 30.

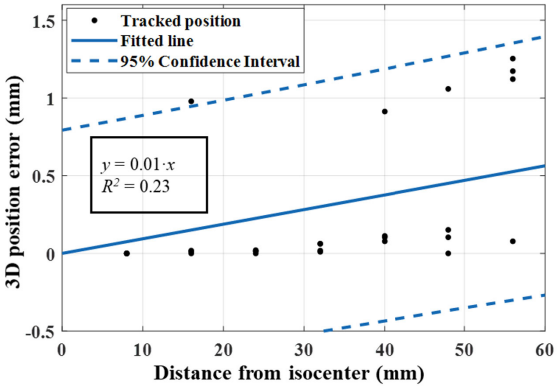

Fig. 13. Calculated marker positional error against its distance from scanner isocenter with the ILI algorithm. A first order linear equation was fitted with a solid line that intercepts at the zero point. The dashed lines represent the 95% confidence interval.

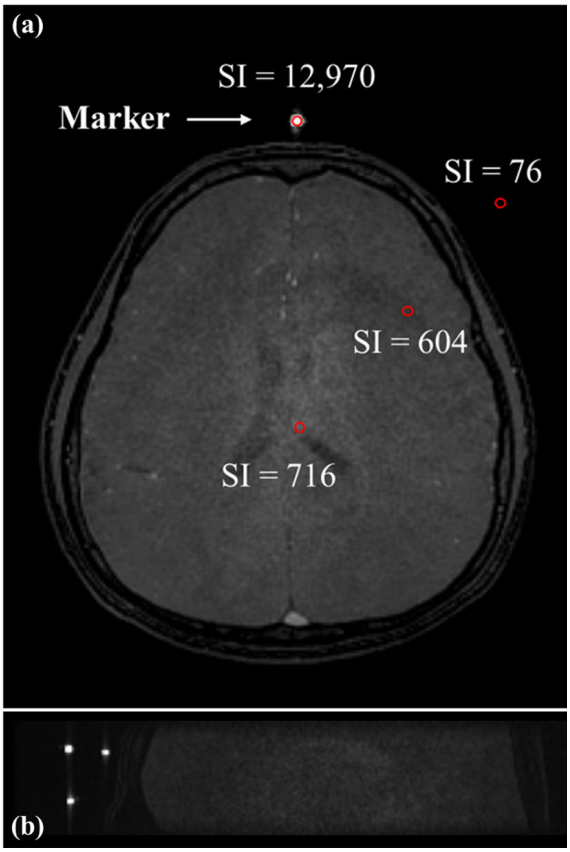

Fig. 14. Low flip-angle (1°) MR scanning image with (a) region of interest average signal intensities (SI) of highlight red region (2 pixel × 2 pixel) indexed. The marker was affixed to a subject's head with a 3D-printed fixture. The average marker signal is about 18 times stronger than the signal from brain, and about 170 times stronger than background noise. (b) Image of the MR-compatible needle guide placed next to the head. Three bright spots can be clearly visualized and identified from the head.

curve in S12 measurement. Thus, the FEA results accurately quantify the coupling effect and resonating modes. Although there are some quantitative differences due to fabrication and assembly tolerance, FEA-based and S12 measured results exhibit almost the same frequency shift trends and curve profiles. **Fig. 10** shows the marker signal intensities at both scanner isocenter and receive coil inner surface. The MR signal was increased by 18 times when marker was offset from the isocenter to the receive coil inner surface.

B. Orientation Dependency

The spectrum of the marker signal in X'-, Y'-, and Z'-direction is shown in **Fig. 11**. The trend of signal change is similar to that obtained with the effective surface modeling shown in (4). The initial signal-to-background ratio is ∼57. Although the marker signal drops when the rotational angle around X'-, and Z'- directions increases, the signal remains bright and can be unambiguously identified from the background, as shown in **Fig. 12**. When θ_X and θ_Y equal 90°, the ratio drops to ∼30.

C. Tracking Accuracy and Precision

MR images with the highest peak-to-noise ratio were used for marker tracking performance analysis. Intensity linear

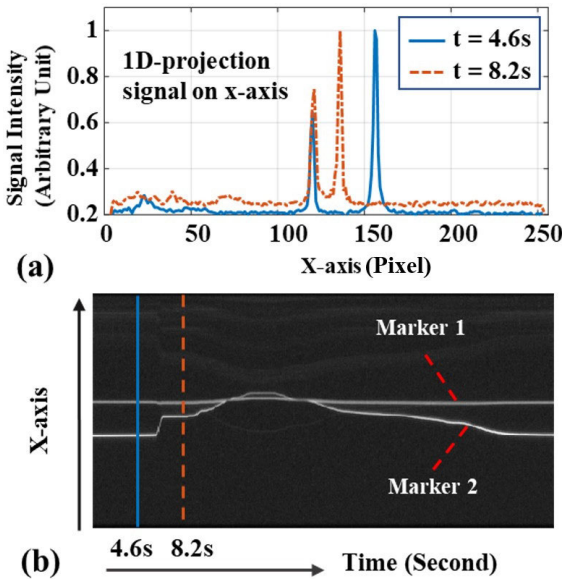

Fig. 15. (a) 1-D projection signal (in X direction) taken from two markers at two different time points. Each peak corresponds to a marker. (b) Continuously projected signal of two markers acquired at 83.3 Hz. The SNR is sufficiently high so that two signal points within −128 mm to +128 mm (with the resolution of 1 mm) can be contrasted and observed at each time stamp.

interpolation algorithm was used to compute the marker position to evaluate its precision. The marker enabled positional localization with a standard deviation of 0.1 mm. Accuracy performance is plotted in **Fig. 13**, showing the relationship of the 3D positional error against the marker position from the isocenter. A first order linear equation $y = 0.01 \cdot x$ can be used to approximate the relationship. Although most positional data fall within 95% confidence level, outlier can be observed and explained by the spatial accuracy of MRI, which has a 1-pixel variance [53]. The 1-pixel variance will lead to 1 mm deviation as the pixel spacing is 1 mm / pixel in current tracking pulse sequence. The 3D positional error increases with further distance from isocenter, which can be explained by multiple (combined) factors, such as MRI scanner $\mathbf{B_0}$ magnetic field inhomogeneity, gradient field nonlinearity, and magnetic susceptibility of the scanned object [54], [55]. The tracking accuracy is comparable to the prior works [7], [32].

D. MR Imaging and Radiofrequency Safety

MR imaging experiments by affixing a tracking marker on a subject's head with a 3D-printed block, and placing a MR-compatible needle guide with 3 markers are shown in **Fig. 14a-b**. The performance plots demonstrate that the signal level from the marker is much higher than the noise from both the head and background (SNR > 18), implying the marker can be easily visualized or tracked both visually and with computer algorithm. One-dimensional (1D) projection readouts from two markers with low flip angle (FA = 1) RF excitation at two timestamps (4.6s, 8.2s) are shown in **Fig. 15a**. Markers' trajectories projected to the X-axis continuously are shown in **Fig. 15b**. MR signals projected from the markers can be contrasted from the background signal at each time stamp at a rate of 83.3 Hz.

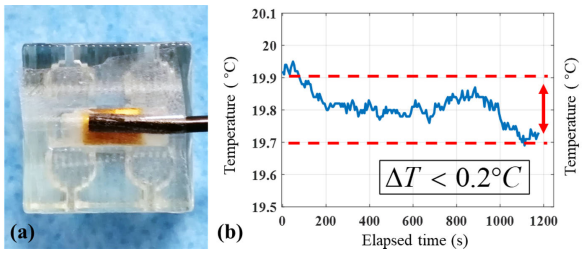

Fig. 16. (a) One fiber-optic fluorescent temperature sensor was affixed to the marker surface. Another temperature sensor was attached to the scanner table as temperature reference. (b) FSE scan applied on the temperature measurement setup for more than 15 min. The temperature was being varied within the range of 0.2 °C.

The temperature measurement setup for the RF safety test is shown in **Fig. 16a**. The recorded maximum change in temperature was less than 0.2 °C as shown in **Fig. 16b**. The heat generated (within 1 °C) is comparable to the prior design of wireless solenoid marker [6]. Before applications of using the marker in contact with the body tissues, it is recommended that additional tests be conducted to identify the potential presence of electrical field hotspots on the marker surface, so as to avoid harmful temperature increases in nearby tissues.

IV. Conclusion and Future Work

This study presents the design, fabrication, and evaluation of a novel MR-based omnidirectional positional marker. The marker's signal can be depicted as a bright spot in any orientation. Although the marker signal was observed to drop by 50% in 2 rotational directions, the signal-to-noise-ratio is still high (>30) which was easily identifiable against the background. Note that the marker has low sensitivity regarding change in $\mathbf{B_1}$ frequency, slice position and field inhomogeneity. The marker sensitivity with respect to the $\mathbf{B_1}$ frequency change is proportional to its quality factor, which is defined by the ratio of center frequency to 3-dB Bandwidth (63.87/22 = 2.9 MHz in our case, as marker has a quality factor of ∼22). Therefore, the sensitivity will reduce by half only if $\mathbf{B_1}$ frequency is shifted substantially by 1.5 MHz (half of 2.9MHz) from 63.87 MHz. Note that the marker sensitivity does not change with respect to slice position as non-selective RF-pulse was utilized. Regarding the effect of field inhomogeneity to the marker intensity, as even 10-ppm field inhomogeneity could only lead to a frequency difference of 638 Hz, which is much lower than the 2.9 MHz bandwidth; therefore, it has negligible effect to the marker intensity.

Our studies have shown that the novel curved marker can provide promising MR-tracking with high quality factor and small form factor. The marker was easy to fabricate and deploy on cylindrical objects (e.g., catheter [56]) comparing to conventional manual wounded markers. The small size and wireless features of the marker simplifies its implementation in different applications. The marker requires no electrical connection or hardware modification to the MRI scanner, thus reducing the barrier for inclusion in both clinical and engineering workflow. The marker is well suited for wireless positional tracking and image-guided interventional procedures. One current limitation is that the marker can only provide omnidirectional tracking and visualization under closed MRI with a circularly polarized (CP) field, but not for open MRI scanners with linearly polarized $\mathbf{B_1}$ field oriented along the cylinder axis. We also plan to investigate if this proposed circuit design can be extended to incorporate on a spherical surface, so as to enable omnidirectional tracking even under open MRI. Future work of the marker will also involve enhancement of the design and fabrication method, improving the consistency of three circuit units, such that the marker can achieve resonance closer to the Larmor frequency. By adopting a multiple layer (i.e., ≥ 4) design, it is possible to further miniaturize the total marker footprint. Tracking pulse sequence can also be optimized to reduce the impact of MRI spatial accuracy to marker tracking performance, such as pixel spacing reduction. $\mathbf{B_1}$ map analysis will be conducted to investigate and quantify the presence and spatial extent of deformation in $\mathbf{B_1}$ field outside the marker which could be detrimental for imaging nearby tissues. We will follow ASTM F2182-09 protocol [57] by adding the saline phantom, and temperature measurement at multiple points, more numbers of fiber-optic probes will be required to measure the temperatures simultaneously in real time.

Acknowledgment

The authors would like to thank Russell H. Taylor and Iulian Iordachita at Johns Hopkins University, who offered their valuable advices on some practical usages and further developments of our proposed work.

References

[1] M. Moche, R. Trampel, T. Kahn, and H. Busse, "Navigation concepts for MR image-guided interventions," *J. Magn. Reson. Imag.*, vol. 27, no. 2, pp. 276–291, Feb. 2008.

[2] A. Alipour, S. Gokyar, O. Algin, E. Atalar, and H. V. Demir, "An inductively coupled ultra-thin, flexible, and passive RF resonator for MRI marking and guiding purposes: Clinical feasibility," *Magn. Reson. Med.*, vol. 80, no. 1, pp. 361–370, Jul. 2018.

[3] Z. Guo et al., "Compact design of a hydraulic driving robot for intraoperative MRI-guided bilateral stereotactic neurosurgery," *IEEE Robot. Autom. Lett.*, vol. 3, no. 3, pp. 2515–2522, Jul. 2018.

[4] F. Bönner et al., "Magnetic resonance guided renal denervation using active tracking: First in vivo experience in swine," *Int. J. Cardiovascular Imag.*, vol. 34, no. 3, pp. 431–439, Mar. 2018.

[5] Y. Chen et al., "Design and fabrication of MR-tracked metallic stylet for gynecologic brachytherapy," *IEEE/ASME Trans. Mechatronics*, vol. 21, no. 2, pp. 956–962, Apr. 2016.

[6] M. B. Ooi, M. Aksoy, J. Maclaren, R. D. Watkins, and R. Bammer, "Prospective motion correction using inductively coupled wireless RF coils," *Magn. Reson. Med.*, vol. 70, no. 3, pp. 639–647, Sep. 2013.

[7] H. Busse, R. Trampel, W. Gründer, M. Moche, and T. Kahn, "Method for automatic localization of MR-visible markers using morphological image processing and conventional pulse sequences: Feasibility for image-guided procedures," *J. Magn. Reson. Imag.*, vol. 26, no. 4, pp. 1087–1096, Oct. 2007.

[8] H. Celik, D. I. Mahcicek, G. A. Wright, and E. Atalar, "Tracking the position and rotational orientation of a catheter using a transmit array system," *IEEE Trans. Med. Imag.*, vol. 32, no. 4, pp. 809–817, Apr. 2013.

[9] M. Rea, D. McRobbie, H. Elhawary, Z. T. H. Tse, M. LampÉrth, and I. Young, "System for 3-D real-time tracking of MRI-compatible devices by image processing," *IEEE/ASME Trans. Mechatronics*, vol. 13, no. 3, pp. 379–382, Jun. 2008.

[10] M. B. Ooi, S. Krueger, W. J. Thomas, S. V. Swaminathan, and T. R. Brown, "Prospective real-time correction for arbitrary head motion using active markers," *Magn. Reson. Med.*, vol. 62, no. 4, pp. 943–954, Oct. 2009.

[11] R. A. Omary et al., "Real-time MR imaging-guided passive catheter tracking with use of gadolinium-filled catheters," *J. Vascular Interventional Radiol.*, vol. 11, no. 8, pp. 1079–1085, Sep. 2000.

[12] O. Unal, J. Li, W. Cheng, H. Yu, and C. M. Strother, "MR-visible coatings for endovascular device visualization," *J. Magn. Reson. Imag.*, vol. 23, no. 5, pp. 763–769, May 2006.

[13] O. Unal, F. R. Korosec, R. Frayne, C. M. Strother, and C. A. Mistretta, "A rapid 2D time-resolved variable-rate *k*-space sampling MR technique for passive catheter tracking during endovascular procedures," *Magn. Reson. Med.*, vol. 40, no. 3, pp. 356–362, Sep. 1998.

[14] C. J. Bakker, R. M. Hoogeveen, J. Weber, J. J. van Vaals, M. A. Viergever, and W. P. Mali, "Visualization of dedicated catheters using fast scanning techniques with potential for MR-guided vascular interventions," *Magn. Reson. Med.*, vol. 36, no. 6, pp. 816–820, Dec. 1996.

[15] D. L. Rubin, A. V. Ratner, and S. W. Young, "Magnetic susceptibility effects and their application in the development of new ferromagnetic catheters for magnetic resonance imaging," *Investigative Radiol.*, vol. 25, no. 12, pp. 1325–1332, Dec. 1990.

[16] S. Patil, O. Bieri, P. Jhooti, and K. Scheffler, "Automatic slice positioning (ASP) for passive real-time tracking of interventional devices using projection-reconstruction imaging with echo-dephasing (PRIDE)," *Magn. Reson. Med.*, vol. 62, no. 4, pp. 935–942, Oct. 2009.

[17] W. R. Nitz, A. Oppelt, W. Renz, C. Manke, M. Lenhart, and J. Link, "On the heating of linear conductive structures as guide wires and catheters in interventional MRI," *J. Magn. Reson. Imag.*, vol. 13, no. 1, pp. 105–114, Jan. 2001.

[18] W. R. Nitz, G. Brinker, D. Diehl, and G. Frese, "Specific absorption rate as a poor indicator of magnetic resonance-related implant heating," *Investigative Radiol.*, vol. 40, no. 12, pp. 773–776, 2005.

[19] A. Buecker, "Safety of MRI-guided vascular interventions," *Minimally Invasive Therapy Allied Technol.*, vol. 15, no. 2, pp. 65–70, Jan. 2006.

[20] E. Atalar et al., "High resolution intravascular MRI and MRS by using a catheter receiver coil," *Magn. Reson. Med.*, vol. 36, no. 4, pp. 596–605, Oct. 1996.

[21] O. Ocali and E. Atalar, "Intravascular magnetic resonance imaging using a loopless catheter antenna," *Magn. Reson. Med.*, vol. 37, no. 1, pp. 112–118, Jan. 1997.

[22] S. Wildermuth, C. L. Dumoulin, T. Pfammatter, S. E. Maier, E. Hofmann, and J. F. Debatin, "MR-guided percutaneous angioplasty: Assessment of tracking safety, catheter handling and functionality," *CardioVascular Interventional Radiol.*, vol. 21, no. 5, pp. 404–410, Sep. 1998.

[23] S. Weiss et al., "In vivo safe catheter visualization and slice tracking using an optically detunable resonant marker," *Magn. Reson. Med.*, vol. 52, no. 4, pp. 860–868, Oct. 2004.

[24] E. Y. Wong, Q. Zhang, J. L. Duerk, J. S. Lewin, and M. Wendt, "An optical system for wireless detuning of parallel resonant circuits," *J. Magn. Reson. Imag.*, vol. 12, no. 4, pp. 632–638, Oct. 2000.

[25] Z. He et al., "Design of a percutaneous MRI-guided needle robot with soft fluid-driven actuator," *IEEE Robot. Autom. Lett.*, vol. 5, no. 2, pp. 2100–2107, Apr. 2020.

[26] Z. Dong et al., "High-performance continuous hydraulic motor for MR safe robotic teleoperation," *IEEE Robot. Autom. Lett.*, vol. 4, no. 2, pp. 1964–1971, Apr. 2019.

[27] K.-H. Lee et al., "MR safe robotic manipulator for MRI-guided intracardiac catheterization," *IEEE/ASME Trans. Mechatronics*, vol. 23, no. 2, pp. 586–595, Apr. 2018.

[28] M. A. Rube et al., "Preclinical feasibility of a technology framework for MRI-guided iliac angioplasty," *Int. J. Comput. Assist. Radiol. Surg.*, vol. 10, no. 5, pp. 637–650, May 2015.

[29] F. Galassi, D. Brujic, M. Rea, N. Lambert, N. Desouza, and M. Ristic, "Fast and accurate localization of multiple RF markers for tracking in MRI-guided interventions," *Magn. Reson. Mater. Phys., Biol. Med.*, vol. 28, no. 1, pp. 33–48, Feb. 2015.

[30] M. A. Rube, A. B. Holbrook, B. F. Cox, J. G. Houston, and A. Melzer, "Wireless MR tracking of interventional devices using phase-field dithering and projection reconstruction," *Magn. Reson. Imag.*, vol. 32, no. 6, pp. 693–701, Jul. 2014.

[31] A. Eldirdiri, F. Courivaud, R. Palomar, P. K. Hol, and O. J. Elle, "Catheter tip tracking for MR-guided interventions using discrete Kalman filter and mean shift localization," *Int. J. Comput. Assist. Radiol. Surg.*, vol. 9, no. 2, pp. 313–322, Mar. 2014.

[32] C.-L. Cheung, J. D. Ho, V. Vardhanabhuti, H.-C. Chang, and K.-W. Kwok, "Design and fabrication of wireless multilayer tracking marker for intraoperative MRI-guided interventions," *IEEE/ASME Trans. Mechatronics*, vol. 25, no. 2, pp. 1016–1025, Apr. 2020.

[33] C. D. Jordan et al., "Wireless resonant circuits printed using aerosol jet deposition for MRI catheter tracking," *IEEE Trans. Biomed. Eng.*, vol. 67, no. 3, pp. 876–882, Mar. 2020.

[34] A. Hai, V. C. Spanoudaki, B. B. Bartelle, and A. Jasanoff, "Wireless resonant circuits for the minimally invasive sensing of biophysical processes in magnetic resonance imaging," *Nature Biomed. Eng.*, vol. 3, no. 1, pp. 69–78, Oct. 2018.

[35] H. H. Quick et al., "Interventional magnetic resonance angiography with no strings attached: Wireless active catheter visualization," *Magn. Reson. Med.*, vol. 53, no. 2, pp. 446–455, 2005.

[36] T. Kuehne, R. Fahrig, and K. Butts, "Pair of resonant fiducial markers for localization of endovascular catheters at all catheter orientations," *J. Magn. Reson. Imag.*, vol. 17, no. 5, pp. 620–624, May 2003.

[37] M. Burl, G. A. Coutts, and I. R. Young, "Tuned fiducial markers to identify body locations with minimal perturbation of tissue magnetization," *Magn. Reson. Med.*, vol. 36, no. 3, pp. 491–493, Sep. 1996.

[38] D. Ellersiek et al., "A monolithically fabricated flexible resonant circuit for catheter tracking in magnetic resonance imaging," *Sens. Actuators B, Chem.*, vol. 144, no. 2, pp. 432–436, Feb. 2010.

[39] R. H. Clark, *Handbook of Printed Circuit Manufacturing*. Dordrecht, The Netherlands: Springer, 1985, p. 620.

[40] M. Mariello et al., "Flexible piezoelectric AlN transducers buckled through package-induced preloading for mechanical energy harvesting," *Nano Energy*, vol. 85, Jul. 2021, Art. no. 105986.

[41] F. W. Grover, *Inductance Calculations*. New York, NY, USA: Dover, 2004.

[42] S. Weiss et al., "Catheter localization using a resonant fiducial marker during interactive MR fluoroscopy," in *Proc. ISMRM*, Philadelphia, PA, USA, 1999, p. 1954.

[43] M. Rea, D. McRobbie, H. Elhawary, Z. T. H. Tse, M. Lamperth, and I. Young, "Sub-pixel localisation of passive micro-coil fiducial markers in interventional MRI," *Magn. Reson. Mater. Phys., Biol. Med.*, vol. 22, no. 2, pp. 71–76, Apr. 2009.

[44] J. Dai et al., "A robotic platform to navigate MRI-guided focused ultrasound system," *IEEE Robot. Autom. Lett.*, vol. 6, no. 3, pp. 5137–5144, Jul. 2021.

[45] W. Wang et al., "Real-time active MR-tracking of metallic stylets in MR-guided radiation therapy," *Magn. Reson. Med.*, vol. 73, no. 5, pp. 1803–1811, May 2015.

[46] T. S. Ibrahim, R. Lee, B. A. Baertlein, A. Kangarlu, and P.-M. L. Robitaille, "Application of finite difference time domain method for the design of birdcage RF head coils using multi-port excitations," *Magn. Reson. Imag.*, vol. 18, no. 6, pp. 733–742, 2000.

[47] D. Ahn and S. Hong, "Effect of coupling between multiple transmitters or multiple receivers on wireless power transfer," *IEEE Trans. Ind. Electron.*, vol. 60, no. 7, pp. 2602–2613, Jul. 2013.

[48] M. E. Stebliy et al., "Vortex dynamics and frequency splitting in vertically coupled nanomagnets," *Sci. Rep.*, vol. 7, no. 1, p. 1127, Apr. 2017.

[49] J. I. Agbinya and H. Nguyen, "Principles and applications of frequency splitting in inductive communications and wireless power transfer systems," *Wireless Pers. Commun.*, vol. 107, no. 2, pp. 987–1017, Jul. 2019.

[50] T. Thabet and J. Woods, "A solution to frequency splitting in magnetic resonance wireless power transfer systems using double sided symmetric capacitors," *Eur. J. Electr. Eng. Comput. Sci.*, vol. 5, no. 2, pp. 6–12, Mar. 2021.

[51] I. R. O. Connell, K. M. Gilbert, M. A. Abou-Khousa, and R. S. Menon, "MRI RF array decoupling method with magnetic wall distributed filters," *IEEE Trans. Med. Imag.*, vol. 34, no. 4, pp. 825–835, Apr. 2015.

[52] H. D. Thanh and J. I. Agbinya, "Investigation and study of mode splitting in near field inductive communication systems," *Int. J. Electron. Telecommun.*, vol. 59, no. 2, pp. 185–194, Jun. 2013.

[53] D. Kondziolka et al., "A comparison between magnetic resonance imaging and computed tomography for stereotactic coordinate determination," *Neurosurgery*, vol. 30, no. 3, pp. 402–407, Mar. 1992.

[54] L. N. Baldwin, K. Wachowicz, S. D. Thomas, R. Rivest, and B. G. Fallone, "Characterization, prediction, and correction of geometric distortion in 3T MR images," *Med. Phys.*, vol. 34, no. 2, pp. 388–399, Feb. 2007.

[55] D. Rotenberg, M. Chiew, S. Ranieri, F. Tam, R. Chopra, and S. J. Graham, "Real-time correction by optical tracking with integrated geometric distortion correction for reducing motion artifacts in functional MRI," *Magn. Reson. Med.*, vol. 69, no. 3, pp. 734–748, Mar. 2013.

[56] Z. Dong et al., "Shape tracking and feedback control of cardiac catheter using MRI-guided robotic platform—Validation with pulmonary vein isolation simulator in MRI," *IEEE Trans. Robot.*, vol. 38, no. 5, pp. 2781–2798, Oct. 2022.

[57] M. Hasegawa, K. Miyata, Y. Abe, and T. Ishigami, "Radiofrequency heating of metallic dental devices during 3.0T MRI," *Dentomaxillofacial Radiol.*, vol. 42, no. 5, May 2013, Art. no. 20120234.